Laser & Photonics Reviews

LASER & PHOTONICS REVIEWS

www.lpr-journal.org

RESEARCH ARTICLE

Coupled Edge-state Modes for Bandgap Engineering and Terahertz Topological Duplexer Integration

Haolong Wang[1] | Hongyu Shi[1] | Zhihao Lan[2] | Wei E. I. Sha[3] | Fei Gao[3] | Zixin Liu[1] | Cheng Guo[1] | Jianjia Yi[1] | Xiaoming Chen[1] | Anxue Zhang[1]

[1]School of Information and Communications Engineering, Xi'an Jiaotong University, Xi'an, China | [2]Department of Electronic and Electrical Engineering, University College London, London, UK | [3]State Key Laboratory of Modern Optical Instrumentation, College of Information Science and Electronic Engineering, Zhejiang University, Hangzhou, China

Correspondence: Hongyu Shi (hongyushi@xjtu.edu.cn)

Received: 19 November 2025 | **Revised:** 11 February 2026 | **Accepted:** 23 February 2026

Keywords: edge state | mode coupling | photonic bandgap | terahertz | topological photonic crystal

ABSTRACT

Topological photonic crystals (TPCs) provide a robust platform for terahertz (THz) applications demanding precise manipulation of topological band structures. This study demonstrates a planar valley TPC operating in the THz regime, facilitating tunable coupling between adjacent edge states. When two domain walls supporting different topological edge modes are positioned in close proximity, the spatial overlap of their evanescent wavefunction tails induces mode coupling, resulting in the emergence of a bandgap within the edge-state continuum. A semi-analytical model, inspired by frameworks in quantum mechanics and condensed matter physics, quantitatively correlates the induced bandgap width with the modal decay constants and spatial separation of the edge states. Full-wave simulations of diverse supercell architectures, including those incorporating Dirac photonic crystals (DPCs), corroborate the theoretical predictions. Exploiting this coupling mechanism, an on-chip THz topological duplexer is designed and experimentally realized, demonstrating low insertion loss, high isolation, and strong immunity to fabrication imperfections, withstanding geometric deviations of up to approximately 20% without performance degradation. These findings establish a unified framework for bandgap engineering via edge-state interactions and open a new avenue toward high-performance, frequency-selective, and integration-compatible topological photonic devices in the THz regime.

1 | Introduction

The terahertz (THz) frequency range has emerged as a promising spectral window for next-generation information technologies owing to its distinctive electromagnetic (EM) characteristics [1–3]. THz waves enable radar sensing, remote imaging, security screening, high-speed communications, and medical diagnostics [4–8], establishing THz technology as a key enabler for future systems. However, its progress remains constrained by substantial transmission loss, inefficient sources, complex fabrication, pronounced dispersion, and limited on-chip scalability [9–11]. Overcoming these challenges demands innovative device concepts that combine low-loss transmission, structural robustness, compact design, and seamless integration.

Topological photonics provides a powerful framework to address these limitations [12–14]. Topological photonic crystals (TPCs) support edge states protected by topological invariants that enable back-scattering-immune EM propagation even in the presence of structural imperfections [15–17]. These properties ensure robust and low-loss transmission while easing fabrication constraints and enhancing integration flexibility [18–20]. Inspired by condensed-matter analogies, early studies on photonic topological phases drew from the quantum Hall effect, leading to

photonic realizations of quantum Hall, spin Hall, and valley Hall states [21–28]. The resulting edge states appear at interfaces between photonic phases of different topological invariants, supporting unidirectional, polarization-locked transport that is resilient to backscattering [29, 30]. On this basis, a wide variety of TPC-based devices have been experimentally demonstrated, such as topological couplers [31, 32], power splitters [33], wavelength-division multiplexers [34–37], topological lasers [38–40], optical delay lines, and antennas [41–44]. These advances further highlight the potential of TPCs for high-frequency communications and integrated photonics [45–47].

Recent progress has greatly advanced the control of band structures and edge-state dynamics in TPCs. Higher-order topological systems have introduced corner and defect-bound states [48–51], while the concurrent breaking of time-reversal symmetry (TRS) and spatial-inversion symmetry (SIS) allows simultaneous spin- and valley-Hall effects within unified platforms [52–54]. Other strategies exploit dislocation- and defect-mediated band engineering [55–57] or co-aligned transverse-electric (TE) and transverse-magnetic (TM) bandgaps to realize polarization-independent operation [58, 59]. Wide domain-wall designs have enabled large-area topological waveguides (TWs) with tunable bandgaps and enhanced flexibility [45, 47, 60, 61].

Despite these advances, the controlled interaction between spatially adjacent edge states at identical frequencies remains insufficiently explored. Such coupling, governed by the overlap of evanescent wavefunctions, is essential for understanding multimode behavior in TPCs. Prior research has primarily focused on mode conversion within a single domain wall [33, 53, 59] or multi-wall systems operating at distinct frequency bands [62, 63]. When two degenerate edge states are brought into close proximity, their interaction can distort the band structure, induce eigenmode hybridization, and alter propagation pathways, effects that become particularly critical in compact, frequency-selective photonic circuits. Moreover, conventional frequency-selective components such as filters and duplexers often exhibit limited out-of-band suppression due to bulk-mode leakage beyond the edge-state regime. Engineering secondary bandgaps within the edge-state continuum through controlled coupling offers a powerful route to enhance signal isolation and device performance.

In this work, a planar valley TPC platform is proposed and experimentally demonstrated to achieve controllable coupling between edge states at identical frequencies. Drawing analogies from condensed-matter and quantum systems, a semi-analytical model (conceptually inspired by tight-binding theory and double-well potential coupling, as shown in Figure 1a,b) is established to describe the underlying mechanism of bandgap formation. As the separation between adjacent domain walls decreases, the spatial overlap of their evanescent edge-state fields increases, inducing strong modal interactions that split degenerate eigenfrequencies and generate a secondary bandgap, as illustrated in Figure 1c. Full-wave simulations and analytical predictions show excellent agreement, and the mechanism is experimentally validated in the THz regime through four distinct configurations of TWs. Building upon this effect, an on-chip topological duplexer is realized, exhibiting high isolation exceeding 30 dB together with strong immunity to fabrication-induced disorder, tolerating geometric deviations of up to approximately 20%. In addition, we observe that the designed TPCs support both trivial and topological modes, and that selective insertion of DPC regions enables their effective modal separation. These findings establish a unified approach for tailoring topological band structures through edge-state interactions and open new pathways toward high-performance, frequency-selective, and integration-ready THz photonic systems.

2 | Results and Discussion

2.1 | Theoretical Modeling of the Coupling of Edge States and Formation of Bandgaps

A single-domain-wall supercell structure permits the emergence of a single edge-state mode within the band structure. These edge-state modes feature EM wavefunctions that remain tightly confined near the domain wall, which decay exponentially along the transverse direction [64]. For typical TPCs, it is commonly agreed that at least four unit-cell layers on either side of the domain wall ($n = 4$) are required to ensure effective spatial isolation of the edge-state fields. Based on this principle, multiple (j) domain walls embedded in a sufficiently wide supercell give rise to j topologically protected transmission channels, each functioning independently. Thus, the entire structure can support j topological edge-state channels. The resulting band structure can then be approximated as a linear superposition of uncoupled edge-state modes, each governed by a single-domain-wall configuration. However, when the spacing between adjacent domain walls falls below the isolation threshold ($n < 4$), significant coupling arises, invalidating the superposition approximation. In this coupling-dominant regime, accurate characterization of the band behavior necessitates a unified modeling approach based on coupled-mode theory.

To analyze the coupling between discrete topological modes, an effective Hamiltonian formalism is employed. Under the weak-coupling approximation, the two spatially adjacent topological edge states can be modeled as a coupled two-level system. The respective wavefunctions of these states are denoted as $\psi_1(y)$ and $\psi_2(y)$, respectively. Under this approximation, the effective Hamiltonian of the system can be formulated as

$$\hat{H}_{\text{eff}} = \begin{pmatrix} \langle \psi_1 \mid \hat{H} \mid \psi_1 \rangle & \langle \psi_1 \mid \hat{H} \mid \psi_2 \rangle \\ \langle \psi_2 \mid \hat{H} \mid \psi_1 \rangle & \langle \psi_2 \mid \hat{H} \mid \psi_2 \rangle \end{pmatrix} \approx \begin{pmatrix} \omega_0 & V \\ V & \omega_0 \end{pmatrix}. \quad (1)$$

Here, the system is assumed to be Hermitian, which holds under negligible material losses and radiative leakage within the operating band, thereby guaranteeing real eigenfrequencies. It is worth noting that this Hermitian approximation is introduced to capture the essential mechanism of coupling-induced mode splitting and bandgap formation. In practical metal-based implementations, non-Hermitian effects associated with ohmic loss and radiation leakage primarily manifest as finite linewidth broadening and insertion loss, rather than altering the qualitative existence or spectral position of the coupling-induced bandgap. The modal fields ψ_1 and ψ_2 are normalized such that

$$\int |\psi_i(\mathbf{r})|^2 \, \mathrm{d}\mathbf{r} = 1 \quad (i = 1, 2), \quad (2)$$

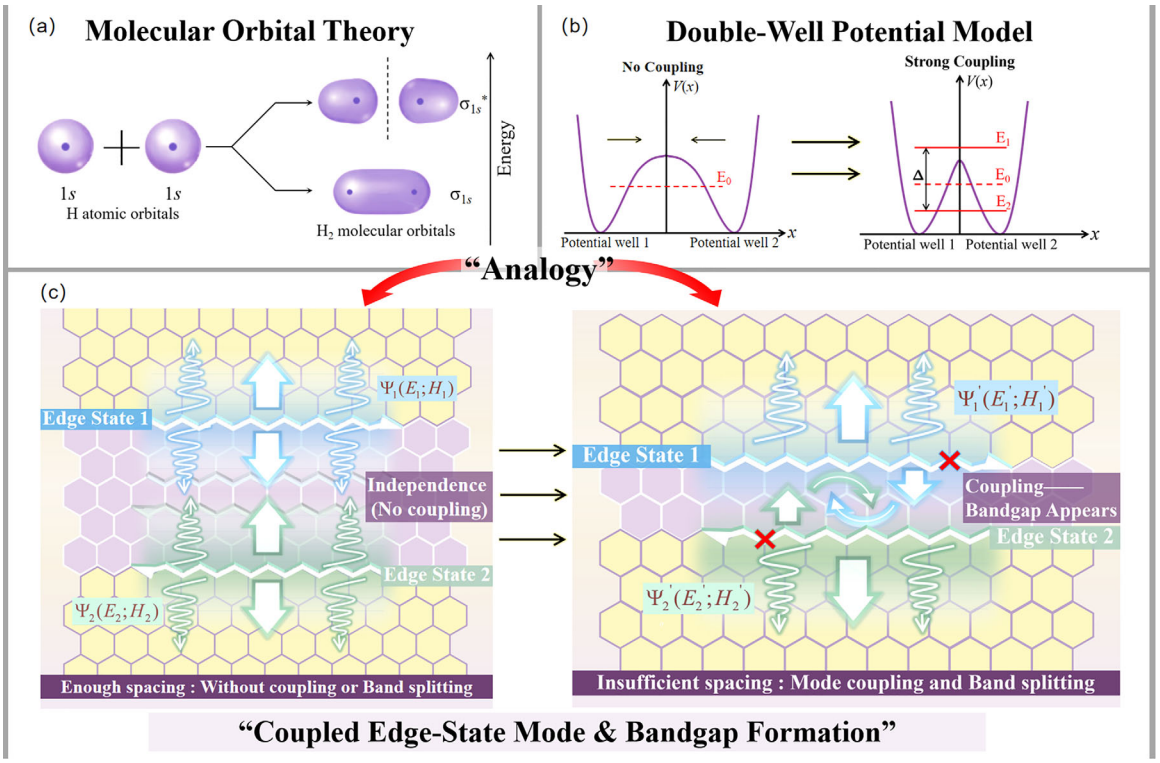

FIGURE 1 | Schematic illustration of the formation of dual edge-state modes and the consequent band evolution caused by mode coupling, along with the analogous models and theoretical frameworks: (a) Molecular orbital model: When two hydrogen atoms combine to form an H_2 molecule, orbital interactions give rise to the formation of bonding and antibonding states with different energies. (b) Double-well potential model: As two isolated potential wells draw closer to each other, level splitting occurs, leading to the emergence of two distinct energy states. (c) Coupled edge-state modes and bandgap formation: When two edge states are spatially far apart, they remain uncoupled; as the distance between them lessens, coupling arises between the edge states, thereby creating a bandgap.

ensuring that the effective Hamiltonian elements $\langle\psi_i|\hat{H}|\psi_j\rangle$ have the dimension of frequency. The parameter ω_0 denotes the degenerate eigenfrequency of the uncoupled edge states. The off-diagonal term V represents the coupling strength, quantifying the energy exchange arising from the overlap of their evanescent wavefunction tails. A nonzero coupling $V \neq 0$ lifts the degeneracy, splitting the modes into two distinct eigenfrequencies. Solving the eigenvalue problem of the effective Hamiltonian yields the corresponding eigenfrequencies as follows:

$$\det(\hat{H} - \omega I) = 0 \tag{3}$$

$$\Rightarrow \quad (\omega_0 - \omega)^2 - V^2 = 0 \tag{4}$$

$$\Rightarrow \quad \omega_{\pm} = \omega_0 \pm V. \tag{5}$$

This result indicates that the two initially degenerate edge-state modes at frequency ω_0 are split through mutual interaction, giving rise to a pair of new eigenmodes located at ω_+ and ω_-. Assuming no other eigenmodes exist within this frequency window, the coupling opens a bandgap between ω_- and ω_+, with a width of $2 \times |V|$. The corresponding eigenstates are symmetric and antisymmetric superpositions of the original edge modes, expressed as

$$\psi_+ = \frac{1}{\sqrt{2}} \times (\psi_1 + \psi_2), \tag{6}$$

$$\psi_- = \frac{1}{\sqrt{2}} \times (\psi_1 - \psi_2). \tag{7}$$

These split frequencies correspond to the symmetric and antisymmetric superpositions of the original edge-state wavefunctions. This simplified two-level Hamiltonian captures the essential physics of edge-state coupling while retaining analytical tractability. The following derivation establishes how this coupling leads to mode splitting and an interaction-induced bandgap. As established in the preceding analysis, the coupling strength directly governs the width of the bandgap induced by the interactions between adjacent edge states. When their separation is sufficiently large, the spatial overlap between the wavefunction tails diminishes, resulting in a vanishing coupling strength $V \to 0$. In this limiting case, the frequency degeneracy is restored, and no bandgap appears in the band diagram. According to standard coupled-mode theory, the coupling strength can be approximated by an overlap integral, where the edge-state wavefunctions are defined as $\psi_1 = \psi_L$ and $\psi_2 = \psi_R$:

$$V = \langle\psi_L \mid \hat{H}_{\text{int}} \mid \psi_R\rangle = \int \psi_L^*(\mathbf{r}) \cdot \hat{H}_{\text{int}} \cdot \psi_R(\mathbf{r})\, d\mathbf{r}. \tag{8}$$

Here, $\psi_L(\mathbf{r})$ and $\psi_R(\mathbf{r})$ denote the eigenmode wavefunctions associated with the left and right edge states, respectively, while $\hat{H}_{int}$ is the perturbative Hamiltonian within the region of spatial overlap. The specific form of $\hat{H}_{int}$ is determined by local structural parameters, such as geometry, permittivity, and refractive index. We assume lossless metallic structures and negligible radiative leakage within the frequency window considered, such that a Hermitian effective Hamiltonian is appropriate. To explicitly evaluate the coupling coefficient V, the standard coupled-mode formalism is employed, where the interaction term arises from the spatial overlap of the two edge-state wavefunctions. In the simplified limit of spatially uniform coupling strength, where $\hat{H}_{int}$ is approximately constant or varies slowly over space, the overlap integral can be further simplified as

$$V \propto \int \psi_L^*(\mathbf{r}) \cdot \psi_R(\mathbf{r})\, d\mathbf{r}, \qquad \text{when } \hat{H}_{int} \text{ is assumed to be constant or varies slowly.} \tag{9}$$

This implies that the coupling strength is directly proportional to the spatial overlap of the two edge-state wavefunctions within the coupling region.

Topological edge states propagate along the domain wall, whereas bulk propagation is suppressed within the primary bandgap. Accordingly, the EM wavefunction is tightly confined near the interface and exhibits exponential decay in the direction perpendicular to propagation [14, 64, 65]. Assuming the domain wall lies along the x-axis, the edge-state wavefunction can be written as

$$\psi(x, y) = Ae^{ik_x x} \cdot e^{-\kappa|y-y_0|}. \tag{10}$$

Here, $\kappa > 0$ denotes the decay constant normal to the domain wall, and y_0 represents the center position of the edge state. The function

$$\psi(y) = Ae^{-\kappa|y-y_0|} \tag{11}$$

characterizes the transverse spatial profile (along y-direction) of the wavefunction. Accordingly, for a configuration supporting two edge states localized at positions $y_{0_L} = 0$ and $y_{0_R} = d$, their respective wavefunctions are expressed as

$$\psi_L(y) = A_L e^{-\kappa_L|y|}, \quad \psi_R(y) = A_R e^{-\kappa_R|y-d|}. \tag{12}$$

In symmetric configurations, $A_L = A_R = A$. The coupling strength $V(d)$ between two edge states separated by a distance d can be formulated as the overlap integral of their wavefunctions along the transverse direction

$$V(d) \propto \int_{-\infty}^{\infty} e^{-\kappa_L|y|} \cdot e^{-\kappa_R|y-d|}\, \mathrm{d}y = \frac{e^{-\kappa_L d} + e^{-\kappa_R d}}{\kappa_L + \kappa_R} + \frac{e^{-\kappa_L d} - e^{-\kappa_R d}}{\kappa_R - \kappa_L} \tag{13}$$

Here, d denotes the center-to-center separation between the two edge states, normalized with respect to the lattice constant a. The parameters κ_L and κ_R represent the transverse decay constants of the edge states associated with the upper and lower domain walls, respectively.

Equation (13) establishes a quantitative relationship among the coupling strength V, the edge-state decay constants κ, and the spatial separation d, and remains valid under the assumption of exponentially confined edge modes. In practical device designs, additional correction factors accounting for crystal geometry and dielectric properties may be necessary to improve the consistency between theoretical predictions, numerical simulations, and experimental measurements. This analytical relation not only provides physical insight into mode coupling between adjacent domain walls but also enables predictive control of edge-state bandgaps through geometric tuning, as confirmed by subsequent full-wave simulations.

2.2 | Geometry and Band Properties of the Planar Valley TPCs

To verify the accuracy of the proposed dual-edge-state coupling model, full-wave simulations are performed on a planar valley TPC featuring a hexagonal lattice (see Figure 2a for the geometric configuration). The design comprises a patterned metallic layer, a metallic ground plane, and a quartz dielectric substrate sandwiched between them. The patterned layer features six circular metallic patches alongside two sets of six metallic grid lines, facilitating both intra-cell and inter-cell connectivity. The lattice constant is $a = 1.351$ mm, and $l = 0.78$ mm denotes the side length of the hexagonal unit cell. The quartz substrate has a thickness of $h = 0.127$ mm and a relative permittivity of $\varepsilon_r = 3.75$. The overall structure thickness is approximately $0.67 \times \lambda$ relative to the operating wavelength.

To modulate the SIS of TPC, four key parameters are defined: R_1 and R_2, representing the radii of the two groups of circular patches, and r_1 and r_2, denoting their displacements relative to the Wannier center. The widths of the metallic grid lines between and within the unit cells are set to $w_1 = w_2 = 0.1 \times l$. Under C_6-symmetry, setting $R_1 = R_2 = 0.2 \times l$, and $r_1 = r_2 = 0.5 \times l$, as shown in Figure 2b, yields a Dirac point degeneracy at the K and K' valleys in the band structure. At this configuration, the unit cell functions as a Dirac Photonic Crystal (DPC), representing the symmetric limit of the proposed TPC. In this configuration, both SIS and TRS are preserved. To break SIS and induce valley topology phase, asymmetry is introduced by setting $R_1 \neq R_2$ and $r_1 \neq r_2$, thereby reducing the symmetry from C_6 to C_3 and lifting the Dirac point degeneracy to open a topological bandgap (see Supporting Information S1 for details). Specifically, $R_1 = 0.3 \times l$, $R_2 = 0.1 \times l$, $r_1 = 0.5 \times l$, and $r_2 = 0.3 \times l$ are chosen, which are corresponding to structural asymmetries of $\Delta R = 0.2 \times l$ and $\Delta r = 0.2 \times l$, as illustrated in Figure 2c. Figure 2d shows the band diagrams of two TPCs, where the red dashed lines and solid lines correspond to the Dirac point being closed and open, respectively.

Two distinct configurations, termed Type-A and Type-B TPCs, are constructed by interchanging the geometric parameters of R_1 and R_2, as well as r_1 and r_2. These configurations exhibit Berry curvature distributions of opposite signs at a given valley, signifying that their valley Chern numbers within the same band are equal in magnitude but opposite in sign. Moreover, each TPC manifests inverted Chern numbers at the K and K' valleys. This dual inversion guarantees the emergence of a pair of topological edge states at their interface, in accordance with the bulk-edge

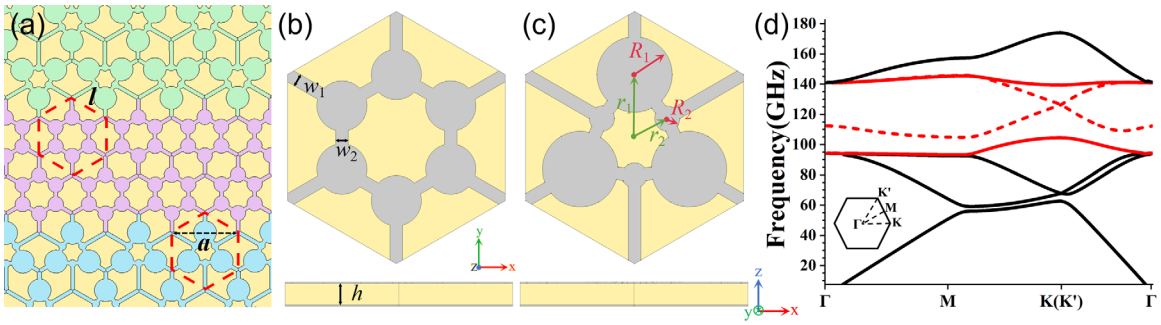

FIGURE 2 | Geometrical configurations and band structures of TPCs: (a) Arrangement of TPCs in a planar lattice, where the purple unit cells denote TPCs with C_6 symmetry and the surrounding ones represent TPCs with C_3 symmetry; (b) Schematic of a TPC structure exhibiting C_6 symmetry; (c) Schematic of a TPC structure exhibiting C_3 symmetry; (d) Band structures of the TPCs calculated over the first Brillouin zone, with the red dashed and solid lines corresponding to the C_6-symmetric and C_3-symmetric TPCs, respectively; Dirac point degeneracy and its lifting at the K (K') valleys can be observed.

correspondence principle. Figure 3a,b illustrates two supercell configurations with distinct domain-wall arrangements, denoted as A-B and B-A supercells, respectively, where the red and purple dashed lines indicate the positions of the domain walls. Each type of domain wall supports one topological edge mode and one trivial mode, as indicated by their corresponding band diagrams. These two modes exhibit nearly identical onset frequencies at the Brillouin-zone boundary while maintaining complete non-overlap across their operating ranges, allowing both to be simultaneously observed in straight-TW configurations. Figure 3c illustrates a composite dual-edge-state supercell incorporating both A-B and B-A domain walls, separated by a single layer ($n = 1$) of Type-B TPC. The corresponding band diagram features four bands, which can be interpreted as the combined projections of the band spectra associated with the two individual domain walls. At the point of band degeneracy, the oppositely directed Poynting vectors of the coupled modes give rise to strong inter-mode coupling, leading to the opening of a distinct bandgap (see Supporting Information S2 for details).

Building upon the analysis of individual topological edge states, the formation and tunability of large-area supercells are further investigated by embedding an intermediate region composed of DPC segments into each domain wall. The corresponding supercell layouts and their band diagrams are shown in Figure 3d,e. By inserting DPCs (highlighted in pink), two extended configurations are constructed, namely the A-C-B and B-C-A supercells. In the associated band diagrams, the topological and trivial bands are consistently highlighted in the same color scheme applied in the preceding figures. Under the influence of the inserted DPCs, a bandgap now emerges between the trivial and topological modes, while the two bands remain fully nonoverlapping across their respective operating ranges; consequently, both modes and the associated bandgap can be clearly observed in straight-TW configurations. A representative dual-edge-state structure is shown in Figure 3f, where the upper and lower interfaces follow an A-C-B and B-C-A arrangements, respectively. A bandgap still emerges near the degenerate frequency, as marked by the purple-shaded region. Comparison of the band structure in Figure 3f with those in Figure 3d,e confirms that the resulting band profile arises from the superposition of the projected state spectra. Consistent with earlier observations, strong mode coupling near the degeneracy point induces the bandgap opening, confirming that the coupling mechanism remains effective even in configurations with wide domain walls.

This section has discussed the band structures of dual-edge-state supercells, in both the absence and the presence of embedded DPCs. In both scenarios, the formation of bandgaps arises from the coupling between adjacent edge states. To complement this analysis, the corresponding eigenmode electric field distributions are provided (see Supporting Information S3 for details). In each case, the number of Type-B TPC layers separating the two domain walls is fixed at $n = 1$. In the subsequent section, the layer number n will be systematically varied for both types of supercells to evaluate the accuracy and predictive capability of the proposed theoretical model.

2.3 | Simulation-Based Validation of Edge-State Coupling Theory

2.3.1 | Coupled Edge States Formed by A-B and B-A Type Domain Walls

To validate the proposed coupling model, full-wave numerical simulations are performed based on the designed TPC platform. The transverse decay profiles of edge states have first been examined by placing electric-field probes within both A-B and B-A domain-wall structures. These probes are aligned along the direction normal to the interface and positioned at consistent relative locations within each unit cell to ensure measurement uniformity and comparability (see Supporting Information S4 for details). The extracted electric field intensity profiles are fitted with exponential decay functions to determine the transverse decay constants of the edge states, yielding $\kappa_L = 1.3454$ for the A-B domain wall and $\kappa_R = 1.2621$ for the B-A domain wall.

Subsequently, a series of supercell structures incorporating two coupled edge states with varying separations are constructed by inserting $n = 1, 2$, or 3 layers of Type-B TPCs between two Type-A regions. These configurations serve to systematically investigate the influence of spatial separation on the coupling behavior. The corresponding band structures are presented in Figure 4a, where the green, blue, and red curves represent the cases with $n = 1, 2$, and 3, respectively. To more clearly visualize the evolution of the

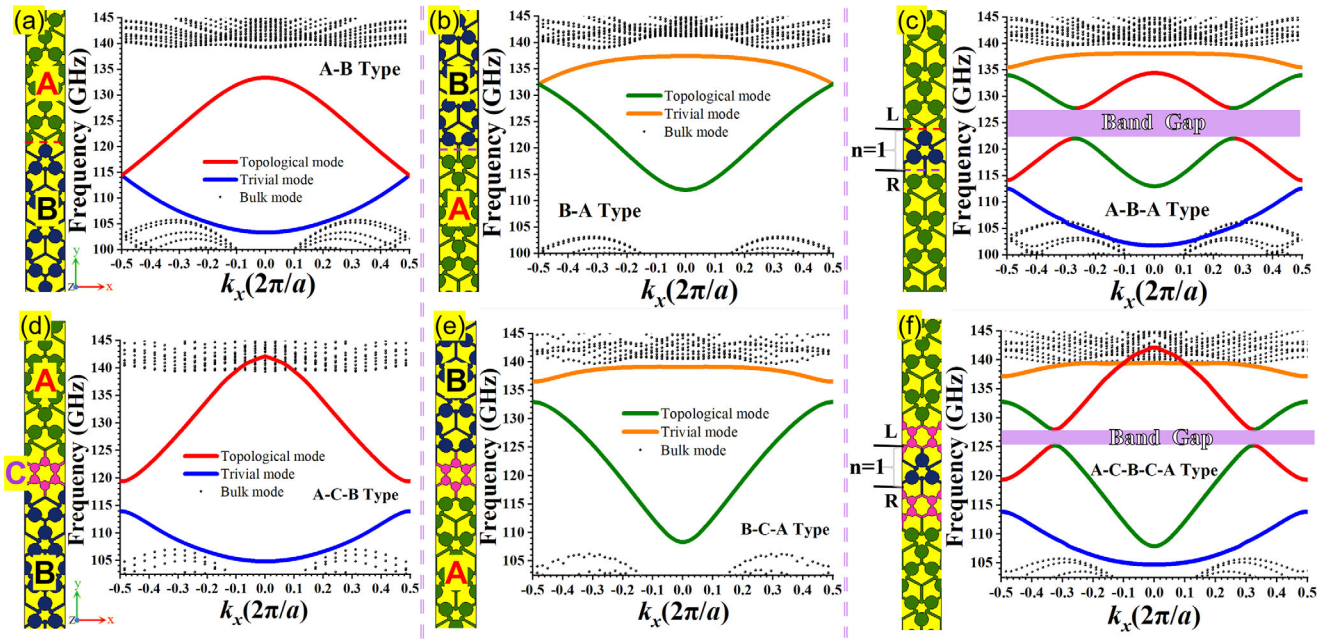

FIGURE 3 | Geometrical configurations and band structures of supercells supporting edge states and dual-edge states: (a) A-B type supercell and its band structure, where one topological edge mode and one trivial mode are identified (The same modal characteristics apply to the remaining band diagrams). (b) B-A type supercell and its band structure; red and purple dashed lines indicate the positions of the domain walls. (c) Dual-edge-state supercell composed of an A-B domain wall on the upper side (red line) and a B-A domain wall on the lower side (purple line), together with its corresponding band structure, where the coupling-induced bandgap is highlighted by the shaded purple region. (d) A-C-B type supercell and its band structure. (e) B-C-A type supercell and its band structure. (f) Dual-edge-state supercell incorporating DPCs, composed of an A-C-B domain wall on the upper side and a B-C-A domain wall on the lower side, together with its corresponding band structure, where the coupling-induced bandgap is highlighted by the shaded purple region.

coupling-induced bandgap, zoomed-in views near the degenerate point are provided in Figure 4i–iii.

To quantify the coupling-induced bandgap, each supercell configuration is evaluated at the band-splitting point (e.g., at $k_x = 0.28$ for the case of $n = 1$). The gap width, defined as $\Delta\omega = 2 \times |V|$, is employed to extract the coupling strengths $V_s(d)$ corresponding to different inter-domain-wall separations. These values are summarized below based on the data from Figure 4a

$$V_s(d) = \begin{cases} 3.420\,, & n = 1; \\ 0.450\,, & n = 2;. \\ 0.078\,, & n = 3; \end{cases} \tag{14}$$

By substituting the fitted decay constants $\kappa_L = 1.3435$ and $\kappa_R = 1.2621$ into Equation (13), the theoretical coupling strengths $V_t(d)$ are obtained and compared with the values extracted numerically. As shown in Figure 4b, the black curve represents the theoretical prediction, while the red dots represent the simulated coupling strengths $V_s(d)$ and the gray dots indicate the discrete theoretical values $V_t(d)$. Despite minor discrepancies are present, the overall trend shows strong agreement, confirming that the theoretical model accurately captures the coupling behavior between adjacent edge states.

When the number of inserted Type-B TPC layers increases to $n = 4$, the resulting separation becomes large enough to suppress observable band splitting within the resolution limits of the current simulation. Under these conditions, the two edge states are effectively decoupled, with the coupling strength approaching $V \approx 0$, and no eigenmode splitting is detected. Figure 4c shows the electric field distributions at the mode-splitting frequencies for these three configurations. In all cases, the field energy is distinctly concentrated between the two domain walls. The upper and lower eigenmodes are predominantly localized near the A-B and B-A domain walls, respectively, consistent with the hybrid mode profiles predicted by Equations (6) and (7).

A key consideration is that the constant prefactor employed in the fitting procedure is determined from the observed bandgap width, yielding a fitted value of $A = 10.635$. In the analytical framework, this constant cannot be calculated explicitly, as it depends on multiple physical parameters, including the lattice constant, the geometric configuration of the TPC, and the relative permittivity. As a result, the coupling strength $V(d)$ in the analytical model can only be expressed as proportional to the overlap integral rather than equated to it

$$\Delta\omega = 2 \times V \propto \text{Overlap}(\kappa_L, \kappa_R, d). \tag{15}$$

2.3.2 | Coupled-Edge-State Supercell with DPCs Composed of A-C-B and B-C-A Type Domain Walls

After validating the coupling model using direct A-B and B-A interfaces, its applicability to dual-edge-state configurations incorporating inserted DPCs is further investigated. Applying a

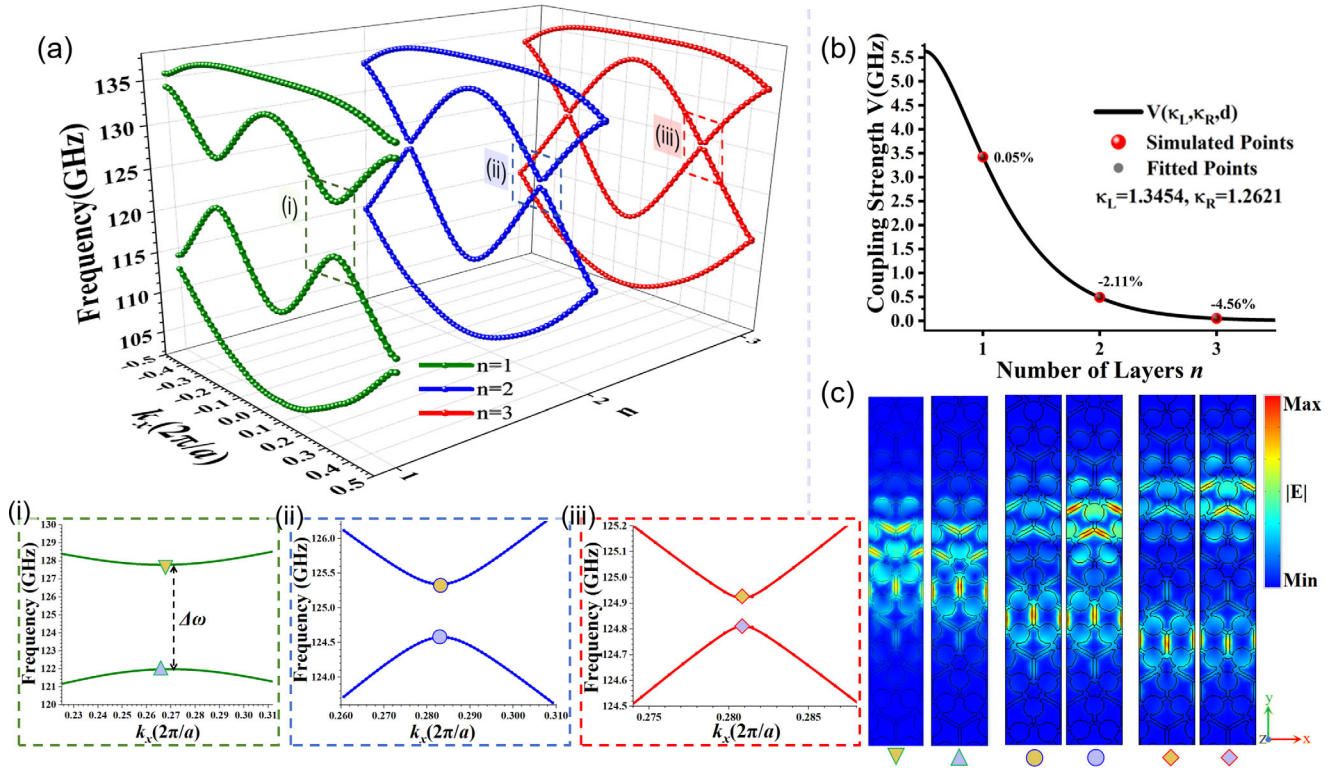

FIGURE 4 | Band diagram evolution and gap variation of dual-edge-state supercells composed of an A-B domain wall at the upper side and a B-A domain wall at the lower side: (a) Band structures of supercells with increasing numbers of intermediate B-type TPC layers ($n = 1, 2$, and 3), represented by green, blue, and red curves, respectively; (i–iii) zoomed-in views of the band diagrams in (a), showing a gradual narrowing of the bandgap as the number of layers increases. (b) Comparison between simulated and theoretical coupling strengths as a function of the number of intermediate B-type layers: red dots represent simulated values of the coupling strength V_s, the black curve denotes the analytical result V_t from the theoretical model, with the relative error annotated. (c) Electric field distribution of the eigenmode near the band splitting point indicated in (i–iii).

similar methodology, the transverse decay constants of the edge states on the A-C-B and B-C-A sides are obtained via exponential fitting, yielding $\kappa_L' = 1.1440$ and $\kappa_R' = 1.0252$, respectively. Following the established analytical framework, a series of supercells are constructed with $n = 1, 2$, and 3 layers of Type-B TPCs. The corresponding band structures are plotted in Figure 5a, where the green, blue, and red curves correspond to $n = 1, 2$, and 3, respectively. To better illustrate the onset and evolution of the coupling-induced bandgap, zoomed-in views around the degenerate point are provided in Figure 5i–iii. The simulation coupling strengths $V_s'(d)$ from Figure 5a are summarized as follows:

$$V_s'(d) = \begin{cases} 1.32\,, & n = 1 \\ 0.26\,, & n = 2\,. \\ 0.04\,, & n = 3 \end{cases} \tag{16}$$

As shown in Figure 5b, the coupling strength $V_t'(d)$ is calculated by substituting the fitted decay constants κ_L' and κ_R' into Equation (13). The theoretical prediction is rigorously compared with the numerically simulated values ($V_s'(d)$), accompanied by an evaluation of relative errors. The strong concordance between theoretical and simulated results substantiates the robustness of the proposed model, even with the insertion of a DPC region with the domain walls. The electric field distribution at the bandgap emergence, depicted in Figure 5c, vividly illustrates the pronounced mutual interaction and coherent coupling of the two edge states.

It is worth noting that, although the duplexer demonstrated in this work does not explicitly exploit large-area topological TW configurations, the analysis of large-area TWs is introduced to support and generalize the theoretical framework developed in this study. Large-area TWs have previously demonstrated their application potential in scenarios such as large-aperture topological antennas and topological power dividers with reconfigurable power ratios.

More importantly, the presented analysis establishes a unified perspective that connects large-area TW construction with the fundamental mechanism of bandgap formation arising from edge-state coupling. This conceptual unification extends the structural design space of TWs and provides a systematic route for bandgap engineering based on modal interactions, enabling enhanced modal selectivity and spectral tunability in future on-chip topological photonic devices.

The dominant source of error originates from the unique field distribution characteristics inherent to the metallic patch-type TPCs employed in this study. In contrast to conventional two-dimensional TPCs that support canonical TE or TM modes, the electric field energy in these structures is predominantly concentrated along the metallic grid lines within each unit cell, whereas

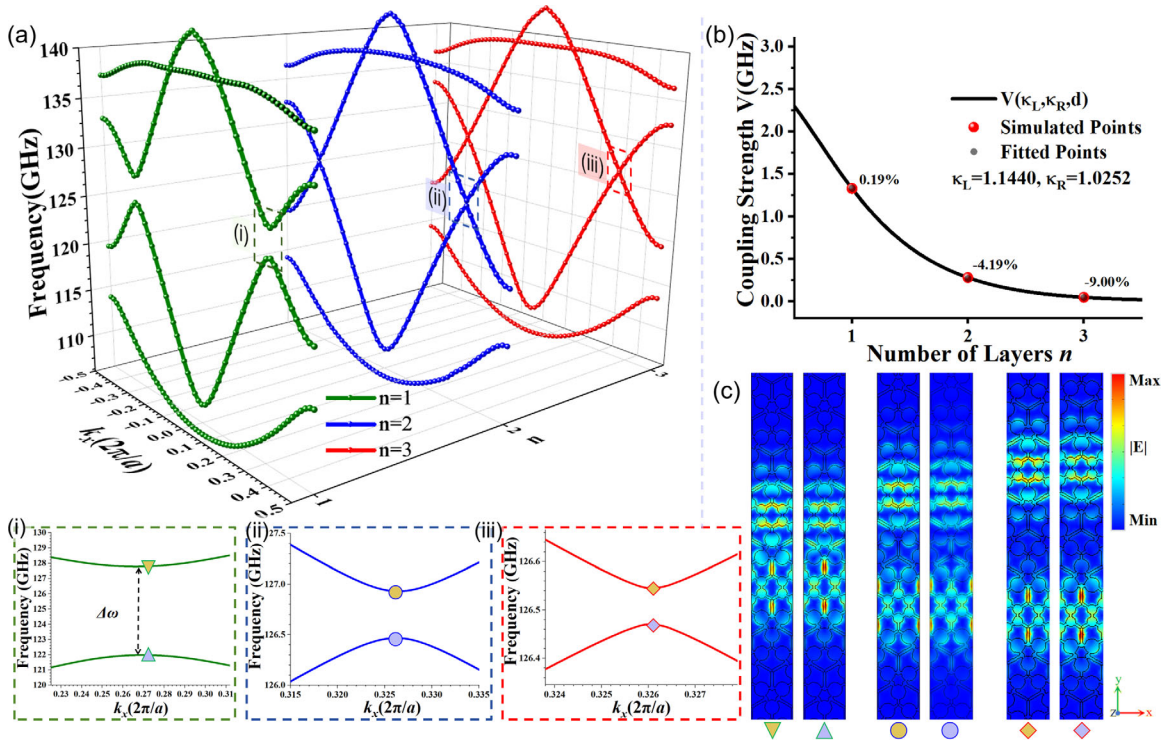

FIGURE 5 | Band diagram evolution and gap variation of dual-edge-state supercells composed of an A-C-B domain wall at the upper side and a B-C-A domain wall at the lower side: (a) Band structures of supercells with increasing numbers of intermediate B-type TPC layers (n= 1, 2, and 3), represented by green, blue, and red curves, respectively; (i–iii) Zoomed-in views of the band diagrams in (a), showing a gradual narrowing of the bandgap as the number of layers increases. (b) Comparison between simulated and theoretical coupling strengths as a function of the number of intermediate B-type layers: red dots represent simulated values of the coupling strength V_s', the black curve denotes the analytical result V_t' from the theoretical model, with the relative error annotated. (c) Electric field distribution of the eigenmode near the band splitting point indicated in (i–iii).

the circular patch regions exhibit significantly attenuated field intensities. This geometry-induced spatial inhomogeneity gives rise to localized field enhancement, resulting in deviations from the idealized exponential decay profile. Consequently, discrepancies may occur during the field amplitude fitting process, thereby compromising the precision of the extracted decay constants.

2.4 | Structure Design and Experimental Demonstration of Topological Duplexer

By leveraging the bandgap induced by edge-state coupling, a compact on-chip topological duplexer operating in the THz regime is designed and realized, as illustrated in Figure 6a. The input signal is fed through Port 1. Port 3 functions as the low-frequency output channel and employs a dual-edge-state TW with a transmission bandwidth spanning from 116.1 to 122.0 GHz. Owing to the coupling-induced bandgap inherent to this dual-edge-state configuration, high-frequency components associated with the other transmission channel are effectively suppressed, thereby ensuring isolation at Port 3. The overall operational bandwidth at Port 1 spans from 110.0 to 133.2 GHz, encompassing both duplexed frequency channels.

Specifically, the TPCs adjacent to Port 2, indicated by the purple and brown TPCs in Figure 6a, are geometrically optimized. As a result, the corresponding B-A type supercell formed by these TPCs supports edge states spanning the frequency range from 122.2 to 136.0 GHz, while a bandgap emerges between 114.2 and 122.2 GHz. Under microstrip-line excitation, the TW constructed by this band structure gives rise to an effective transmission window of 126.0–130.7 GHz.

Similarly, the TPCs surrounding Port 3, highlighted by the light-blue and light-green regions, are subject to minor geometric tuning. Although these adjustments are not essential to the underlying operating principle of the device, they contribute to improved in-band flatness of the transmission response (see Supporting Information S5 for details).

Upon excitation with a broadband input signal at Port 1, frequency-selective spatial separation is observed within the region highlighted by the red circle in Figure 6a. The low-frequency components are directed toward Port 3 along the red-indicated propagation path, whereas the high-frequency components are guided to Port 2 following the black-arrow trajectory. At low frequencies, the EM energy preferentially propagates leftward along the dual-edge-state waveguide, following the path indicated by the red arrows in Figure 6a. In this regime, coupling into the opposite branch is strongly suppressed, as the corresponding supercell of the high-frequency channel exhibits a bandgap that prohibits further rightward transmission, thereby ensuring effective isolation at Port 2.

Conversely, at high frequencies, propagation along the original dual-edge-state channel is inhibited by the coupling-induced

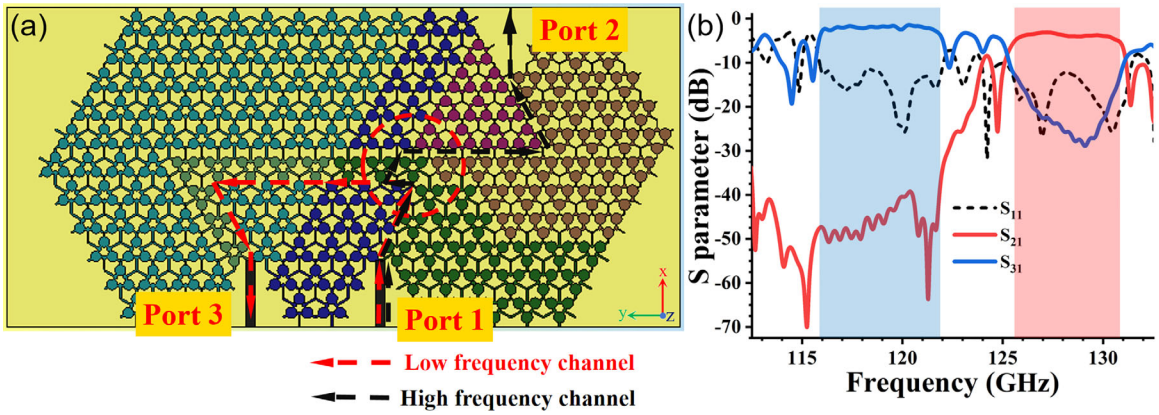

FIGURE 6 | Structure and simulated performance of the topological duplexer: (a) Geometric layout of the topological duplexer, where Port 1 serves as the common port; at the intersection junction marked by red circle, low-frequency and high-frequency signals propagate along the red and black arrows, respectively; (b) Simulated S-parameters.

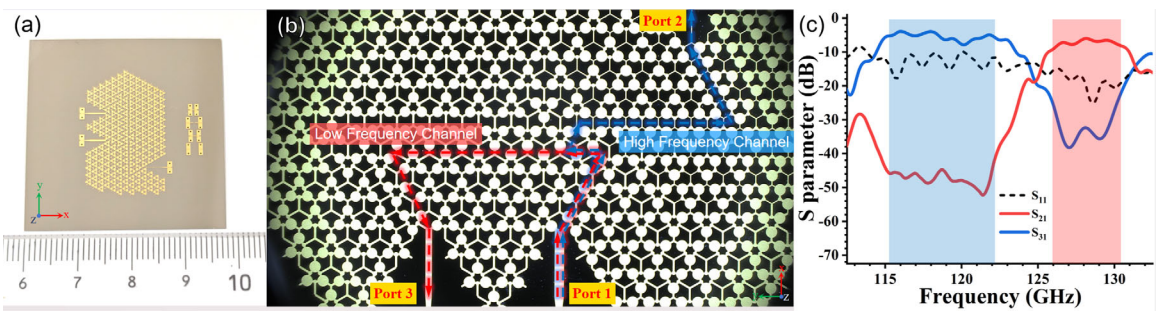

FIGURE 7 | Experimental demonstration and measured performance of the topological duplexer: (a) Photograph of the fabricated prototype; (b) Microscope image of the device under test on the probe station, where the low-frequency and high-frequency channels are indicated by red and blue dashed lines, respectively. (c) Measured S-parameters.

bandgap. As a result, the incident energy is redirected into the opposite branch and guided along the path marked by the black arrows. Owing to the chiral nature of the topological edge states, back-propagation toward the left is forbidden, and the energy is instead funneled toward Port 2, thereby realizing isolation at Port 3 (see Supporting Information S6 for details).

Figure 6b presents the simulated S-parameters of the duplexer. Across both operational frequency bands, the reflection coefficient S_{11} remains consistently below −11 dB, demonstrating effective impedance matching at the input port and efficient coupling of the signal from the microstrip line into the TW with minimal reflection loss.

Within the low-frequency passband, signal energy is predominantly directed from Port 1 to Port 3, exhibiting an insertion loss below 2.8 dB ($|S_{31}| \leq 2.8$ dB), indicative of efficient guided-wave propagation. Concurrently, the isolation at Port 2 exceeds 40 dB across the entire band, peaking at 64 dB, which reflects strong suppression of out-of-band leakage. In the high-frequency regime, the signal is routed from Port 1 to Port 2 with an insertion loss maintained below 4.5 dB ($|S_{21}| \leq 4.5$ dB). Port 3 achieves an isolation maximum of 31 dB, and sustains isolation levels above 22 dB throughout the operating range (see Supporting Information S6 for details). These performance metrics confirm that the duplexer delivers low insertion loss, high inter-port isolation, and negligible back-reflection across both frequency bands, thereby validating the effectiveness of coupling-induced bandgaps for compact and integrable photonic routing applications.

Figure 7a presents the schematic of the fabricated topological duplexer for experimental validation. The device is fabricated on a silicon substrate by depositing a copper layer, followed by patterning with standard photolithography and subsequent etching to define the circuit structures. To ensure efficient connection with the ground-signal-ground (GSG) probes, each port is designed with a normalized impedance and equipped with dual ground pads for reliable grounding (see Supporting Information S7 for details). The device is characterized using a millimeter-wave probe station (model: MPN-600L), equipped with WR-6 waveguide GSG Accutera Probes operating from 110 to 170 GHz, which matches the designed working band of the device. The probe configuration is consistent with that reported in [66].

Figure 7b shows a photograph of the thin-film circuit captured under the probe station, where the red and blue dashed lines indicate the signal paths of the low- and high-frequency channels, respectively (see Supporting Information S8 for details). Figure 7c illustrates the measured transmission characteristics

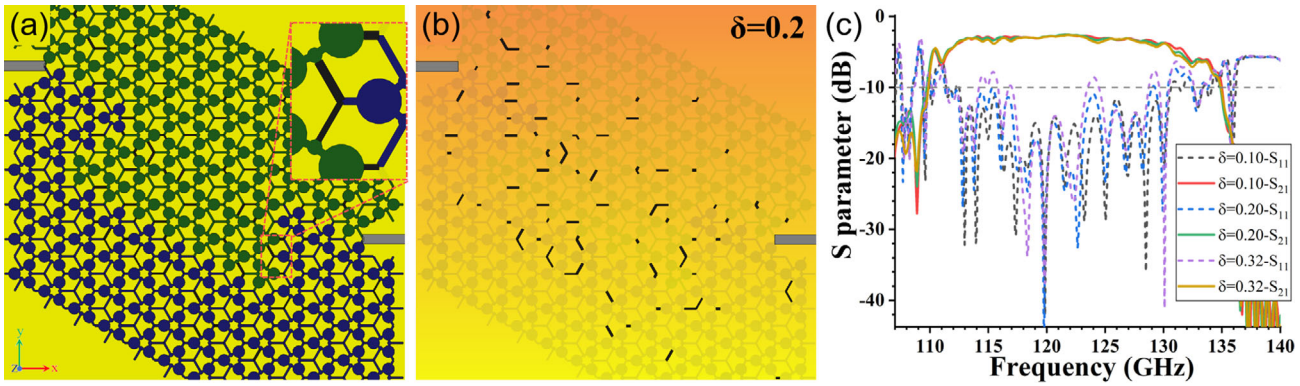

FIGURE 8 | Numerical evaluation of topological robustness under fabrication-induced geometric disorder: (a) Bent TW with intentionally introduced random defects, where the widths of selected metal interconnects in the TPC are locally increased or reduced to emulate realistic fabrication tolerances; (b) Schematic illustration of the locations of the perturbed metal interconnects, highlighted to indicate the regions where geometric deviations are applied; (c) Simulated S-parameters of the bent TW for different levels of relative geometric deviation δ, corresponding to $\delta = 0.10$, 0.2, and 0.32.

of the duplexer, which exhibit excellent agreement with the simulated results. The low- and high-frequency channels operate from 115.5 to 122.1 GHz and from 126.0 to 130.4 GHz, respectively, with return losses better than -10 dB and isolation levels of 43 dB and 30 dB. These experimental results confirm the expected duplexing functionality and further validate the feasibility of the band-coupling-based design strategy for topological filter devices.

The demonstrated duplexer substantiates the viability of engineering bandgaps via coupling-induced splitting between adjacent edge states. By adjusting the spatial configuration of edge-state modes with distinct decay constants and spectral alignments, both the central frequency and bandwidth of the resulting bandgap can be precisely modulated. This coupling-based mechanism provides a flexible and robust design paradigm for frequency-selective topological components and enables adaptive integration within next-generation photonic systems.

2.5 | Evaluation of Topological Robustness

Topological robustness is one of the key advantages that distinguishes TWs from conventional circuit architectures. To experimentally and numerically verify the tolerance of the proposed TPC design to fabrication inaccuracies, substantial and randomly distributed geometric perturbations are intentionally introduced into the metal interconnect widths of a bent TW, as illustrated in Figure 8. The relative geometric deviation is quantified by a dimensionless parameter

$$\delta = \frac{\Delta w}{w_1}, \tag{17}$$

where w_1 denotes the width of metallic grid lines between unit cells and Δw represents the imposed dimensional variation.

Figure 8a shows the configuration of the bent waveguide, which consists of two consecutive sharp Z-shaped bends. The locations with introduced artificial defects are marked by black lines in Figure 8b, corresponding to a representative dimensional deviation of $\delta = 0.2$. As δ increases, the return loss of the TW gradually degrades. The simulated S-parameters of the bent waveguide under different error levels of δ are presented in Figure 8c. Notably, even when δ reaches up to 0.2, the return loss remains below −10 dB, demonstrating a level of robustness that significantly exceeds that of conventional microstrip-based circuits.

In addition to continuous geometric perturbations, the defect robustness of the TWs is further evaluated by introducing representative fabrication-induced imperfections, including metal bridging, geometric disorder, and localized material omissions. Full-wave simulations confirm that these structural defects exert negligible influence on the transmission characteristics, thereby validating the intrinsic topological protection of the proposed waveguide against typical manufacturing imperfections (see Supporting Information S9 for details).

3 | Conclusion

In summary, a planar valley TPC platform is established for tunable bandgap engineering via controlled coupling between adjacent edge states. When edge-state modes with distinct field distributions and decay characteristics are brought into proximity, their evanescent wavefunctions tails spatially overlap. This interaction lifts the intrinsic frequency degeneracy, resulting in a controllable bandgap within the edge-state continuum. A semi-analytical model, inspired by quantum-mechanical principles, quantitatively links the coupling strength to the decay constants and spatial separation, in good agreement with full-wave simulations. To demonstrate scalability and structural flexibility, DPC layers are introduced to form large-area TWs, enabling reconfigurable and multifunctional implementations. Leveraging this framework, a THz-band on-chip topological duplexer is experimentally realized, achieving low insertion loss and high inter-port isolation. Collectively, these findings establish a generalized and scalable strategy for bandgap modulation through edge-state interactions, paving the way for the development of compact, reconfigurable, and integration-ready topological photonic devices.

4 | Experimental Section

The topological duplexers were fabricated on square quartz substrates ($\varepsilon_r = 3.75$, thickness = 0.127 mm) with a side length of 3.86 cm. A 1 μm-thick copper layer was deposited via electron-beam evaporation and patterned by standard photolithography and wet etching, achieving a minimum feature size of 0.4 μm. A continuous copper film was formed on the backside of the substrate to serve as the ground plane.

The measurement setup comprised a millimeter-wave probe station (model: MPN-600L) equipped with WR-6 waveguide GSG Accutera Probes operating from 110 to 170 GHz, and connected to a vector network analyzer (model: Ceyear 3674PA) with two Ceyear 3601Q frequency-extension modules (110 - 170 GHz). Thru-Reflect-Line (TRL) calibration was performed prior to testing to remove systematic errors from cables and probes. The S-parameters between ports 1-2 and 1-3 were recorded to evaluate transmission efficiency and isolation performance. All measurements were conducted at room temperature under stable probe contact conditions.

A multi-software simulation workflow was implemented to guide device design and theoretical verification. Time-domain simulations of the TWs and duplexer were performed in CST Studio Suite 2020 to optimize structural parameters and frequency responses. The unit-cell and supercell band structures and eigenmodes were calculated using COMSOL Multiphysics 5.5. The Chern numbers were evaluated with COMSOL 6.2 and MATLAB R2022b based on the simulated eigenmodes to confirm the nontrivial topological characteristics of the device.

Conflicts of Interest

No. The authors declare no conflict of interest.

Data Availability Statement

The data that support the findings of this study are available in the supplementary material of this article.

References

1. Y. Lampert, A. Shams-Ansari, and A. Gaier, "Photonics-Integrated Terahertz Transmission Lines," *Nature Communications* 16 (2025): 7004, https://doi.org/10.1038/s41467-025-62267-y.

2. I. F. Akyildiz, J. M. Jornet, and C. Han, "Terahertz band: Next Frontier for Wireless Communications," *Physical Communication* 12 (2014): 16–32, https://www.sciencedirect.com/science/article/pii/S1874490714000238.

3. K. Sengupta, T. Nagatsuma, and D. M. Mittleman, "Terahertz Integrated Electronic and Hybrid Electronic–Photonic Systems," *Nature Electronics* 1, no. 12 (2018): 622–635, https://doi.org/10.1038/s41928-018-0173-2.

4. M. Tonouchi, "Cutting-Edge Terahertz Technology," *Nature Photonics* 1, no. 2 (2007): 97–105, https://doi.org/10.1038/nphoton.2007.3.

5. H. Pakarzadeh, S. Rezaei, and L. Namroodi, "Hollow-Core Photonic Crystal Fibers for Efficient Terahertz Transmission," *Optics Communications* 433 (2019): 81–88.

6. B. Ferguson and X. C. Zhang, "Materials for Terahertz Science and Technology," *Nature Materials* 1 (2002): 26–33, https://doi.org/10.1038/nmat708.

7. M. Zhan, J. Wu, Y. Li, G. Xu, and Y. Zhu, "An Adaptive Nonlinear Phase Error Estimation and Compensation Method for Terahertz Radar Imaging System," *IEEE Journal on Miniaturization for Air and Space Systems* 5, no. 2 (2024): 108–116.

8. M. Bonmann, A. Moradikouchi, T. Bryllert, et al., "Terahertz Radar Observes Powder Dynamics for Pharmaceutical Manufacturing," *IEEE Sensors Journal* 24, no. 13 (2024): 20512–20522.

9. P. Shumyatsky and R. R. Alfano, "Terahertz Sources," *Journal of Biomedical Optics* 16, no. 3 (2011): 033001, https://doi.org/10.1117/1.3554742.

10. Q. J. Gu, "Thz Interconnect: The Last Centimeter Communication," *IEEE Communications Magazine* 53, no. 4 (2015): 206–215.

11. M. A. Habib, M. S. Anower, L. F. Abdulrazak, and M. S. Reza, "Hollow Core Photonic Crystal Fiber for Chemical Identification in Terahertz Regime," *Optical Fiber Technology* 52 (2019): 101933, https://www.sciencedirect.com/science/article/pii/S1068520019300458.

12. Z. Wang, Y. Chong, J. D. Joannopoulos, and M. Soljacic, "Observation of Unidirectional Backscattering-Immune Topological Electromagnetic States," *Nature* 461, no. 7265 (2009): 772–775.

13. L. Lu, J. D. Joannopoulos, and M. Soljacic, "Topological Photonics," *Nature Photonics* 11, no. 8 (2014): 821–829.

14. X. Ni, S. Yves, A. Krasnok, and A. Alu, "Topological Metamaterials," *Chemical Reviews* 123, no. 12 (2023): 7585–7654.

15. X. T. He, E. T. Liang, and J. J. Yuan, "A Silicon-on-Insulator Slab for Topological Valley Transport," *Nature Communications* 10 (2019): 872, https://doi.org/10.1038/s41467-019-08881-z.

16. Y. Yang, Y. F. Xu, T. Xu, et al., "Visualization of a Unidirectional Electromagnetic Waveguide Using Topological Photonic Crystals Made of Dielectric Materials," *Physical Review Letters* 120 (2018): 217401, https://link.aps.org/doi/10.1103/PhysRevLett.120.217401.

17. W. Yan, R. Chen, W. Liu, Y. Tan, Y. Kivshar, and F. Chen, "Tunable Edge States and Topological Solitons in Non-Hermitian Photonic Lattices," *Laser & Photonics Reviews* 19, no. 15 (2025): 2402126, https://onlinelibrary.wiley.com/doi/abs/10.1002/lpor.202402126.

18. X. Cheng, C. Jouvaud, and X. Ni, "Robust Reconfigurable Electromagnetic Pathways Within a Photonic Topological Insulator," *Nature Materials* 15 (2016): 542–548, https://doi.org/10.1038/nmat4573.

19. F. Gao, H. Xue, Z. Yang, et al., "Topologically Protected Refraction of Robust Kink States in Valley Photonic Crystals," *Nature Physics* 14 (2018): 140–144, https://doi.org/10.1038/nphys4304.

20. M. I. Shalaev, W. Walasik, and A. Tsukernik, "Robust Topologically Protected Transport in Photonic Crystals at Telecommunication Wavelengths," *Nature Nanotechnology* 14 (2019): 31–34, https://doi.org/10.1038/s41565-018-0297-6.

21. L.-H. Wu and X. Hu, "Scheme for Achieving a Topological Photonic Crystal by Using Dielectric Material," *Physical Review Letters* 114 (2015): 223901, https://link.aps.org/doi/10.1103/PhysRevLett.114.223901.

22. C. He, X.-C. Sun, X.-P. Liu, et al., "Photonic Topological Insulator With Broken Time-Reversal Symmetry," *Proceedings of the National Academy of Sciences* 113, no. 18 (2016): 4924–4928, https://www.pnas.org/doi/abs/10.1073/pnas.1525502113.

23. T. Ma and G. Shvets, "All-Si Valley-Hall Photonic Topological Insulator," *New Journal of Physics* 18, no. 2 (2016): 025012, https://dx.doi.org/10.1088/1367-2630/18/2/025012.

24. Y. Kang, X. Ni, and X. Cheng, "Pseudo-Spin–Valley Coupled Edge States in a Photonic Topological Insulator," *Nature Communications* 9 (2018): 3029, https://doi.org/10.1038/s41467-018-05408-w.

25. X. Wu, Y. Meng, and J. Tian, "Direct Observation of Valley-Polarized Topological Edge States in Designer Surface Plasmon Crystals," *Nature Communications* 8 (2017): 1304, https://doi.org/10.1038/s41467-017-01515-2.

26. H. Xue, Y. Yang, and B. Zhang, "Topological Valley Photonics: Physics and Device Applications," *Advanced Photonics Research* 2, no. 8 (2021): 2100013, https://onlinelibrary.wiley.com/doi/abs/10.1002/adpr.202100013.

27. J. Ma, X. Xi, and X. Sun, "Topological Photonic Integrated Circuits Based on Valley Kink States," *Laser & Photonics Review* 13, no. 12 (2019): 1900087, https://onlinelibrary.wiley.com/doi/abs/10.1002/lpor.201900087.

28. Z. Lan, M. L. N. Chen, J. W. You, and W. E. I. Sha, "Large-Area Quantum-Spin-Hall Waveguide States in a Three-Layer Topological Photonic Crystal Heterostructure," *Physical Review A* 107 (2023): L041501, https://link.aps.org/doi/10.1103/PhysRevA.107.L041501.

29. H. Wang, L. Sun, J. Li, et al., "Refraction and Coupling of Topological Edge State Based on Silicon Valley Photonic Crystals," *Laser & Photonics Reviews* 19, no. 12 (2025): 2401627, https://onlinelibrary.wiley.com/doi/abs/10.1002/lpor.202401627.

30. C. H. Guo, G. J. Tang, M. Y. Li, W. J. Chen, X. T. He, and J. W. Dong, "Quantifying Robustness Against Sharp Bending in an Integrated Topological Interface of Valley Photonic Crystals," *Nanophotonics* 13, no. 8 (2024): 1387–1395, https://doi.org/10.1515/nanoph-2023-0727.

31. G. Tang, X. Chen, and L. Sun, "Broadband and Fabrication-Tolerant 3-db Couplers With Topological Valley Edge Modes," *Light: Science & Applications* 13 (2024): 166.

32. Y. Li, M. Jung, Y. Yu, Y. Han, B. Zhang, and G. Shvets, "Topological Directional Coupler," *Laser & Photonics Reviews* 18, no. 11 (2024): 2301313, https://onlinelibrary.wiley.com/doi/abs/10.1002/lpor.202301313.

33. X. T. He, C. H. Guo, G. J. Tang, M. Y. Li, X. D. Chen, and J. W. Dong, "Topological Polarization Beam Splitter in Dual-Polarization All-Dielectric Valley Photonic Crystals," *Physical Review Applied* 18 (2022): 044080, https://link.aps.org/doi/10.1103/PhysRevApplied.18.044080.

34. L. He, Z. Lan, Y. Yang, et al., "Wavelength Division Multiplexing Based on the Coupling Effect of Helical Edge States in Two-Dimensional Dielectric Photonic Crystals," *Optics Express* 32, no. 7 (2024): 11259–11270, https://opg.optica.org/oe/abstract.cfm?URI=oe-32-7-11259.

35. K. Xu, Z. Xiao, X. Deng, G. Xie, M. Fang, and Z. Huang, "Topology Optimization-Based Design of Topological Edge-State Wavelength Division Multiplexer," *IEEE Photonics Technology Letters* 35, no. 14 (2023): 773–776.

36. G. J. Tang, X. D. Chen, F. L. Shi, J. W. Liu, M. Chen, and J. W. Dong, "Frequency Range Dependent Topological Phases and Photonic Detouring in Valley Photonic Crystals," *Physical Review B* 102 (2020): 174202, https://link.aps.org/doi/10.1103/PhysRevB.102.174202.

37. H. Wang, H. Shi, W. E. I. Sha, et al., "Design of High-Isolation Topological Duplexer Utilizing Dual-Edge State Topological Waveguides," *IEEE Transactions on Antennas and Propagation* 72, no. 11 (2024): 8802–8809.

38. Y. Zeng, U. Chattopadhyay, B. Zhu, et al., "Electrically Pumped Topological Laser With Valley Edge Modes," *Nature* 578, no. 7794 (2020): 246–250.

39. S. Zhao, W. Zhao, L. Shi, Y. Han, Y. Cui, and G. Li, "High-q Two-Dimensional Perovskite Topological Laser," *Optics Express* 32, no. 4 (2024): 6258–6265, https://opg.optica.org/oe/abstract.cfm?URI=oe-32-4-6258.

40. H. Zhong, Y. Li, D. Song, et al., "Topological Valley Hall Edge State Lasing," *Laser & Photonics Reviews* 14, no. 7 (2020): 2000001, https://onlinelibrary.wiley.com/doi/abs/10.1002/lpor.202000001.

41. Z. Xu, M. Wang, S. Fang, H. Liu, Z. Wang, and D. F. Sievenpiper, "Broadside Radiation From Chern Photonic Topological Insulators," *IEEE Transactions on Antennas and Propagation* 70, no. 3 (2022): 2358–2363.

42. Z. Zhang, Y. Tian, Y. Wang, et al., "Directional Acoustic Antennas Based on Valley-Hall Topological Insulators," *Advanced Materials* 30, no. 36 (2018): 1803229.

43. R. Jia, S. Kumar, T. C. Tan, et al., "Valley-Conserved Topological Integrated Antenna for 100-gbps thz 6g Wireless," *Science Advances* 9, no. 44 (2023): eadi8500, https://www.science.org/doi/abs/10.1126/sciadv.adi8500.

44. H. Wang, H. Shi, W. E. I. Sha, et al., "Terahertz High-Gain Leaky-Wave Antenna Utilizing Valley Topological Photonic Crystals With Line Defects," *Journal of Physics D: Applied Physics* 58, no. 21 (2025): 215104, https://doi.org/10.1088/1361-6463/add023.

45. M. L. N. Chen, L. J. Jiang, Z. Lan, and W. E. I. Sha, "Pseudospin-Polarized Topological Line Defects in Dielectric Photonic Crystals," *IEEE Transactions on Antennas and Propagation* 68, no. 1 (2020): 609–613.

46. Q. Chen, L. Zhang, M. He, et al., "Valley-Hall Photonic Topological Insulators With Dual-Band Kink States," *Advanced Optical Materials* 7, no. 15 (2019): 1900036, https://onlinelibrary.wiley.com/doi/abs/10.1002/adom.201900036.

47. X. Yu, J. Chen, Z. Y. Li, and W. Liang, "Topological Large-Area One-Way Transmission in Pseudospin-Field-Dependent Waveguides Using Magneto-Optical Photonic Crystals," *Photonics Research* 11, no. 11 (2023): 1105, https://www.researching.cn/articles/OJa2c8c76f0cd35889.

48. Z. Xiong, Z. K. Lin, H. X. Wang, et al., "Corner States and Topological Transitions in Two-Dimensional Higher-Order Topological Sonic Crystals With Inversion Symmetry," *Physical Review B* 102 (2020): 125144, https://link.aps.org/doi/10.1103/PhysRevB.102.125144.

49. Y. Zhao, F. Liang, J. Han, X. Wang, D. Zhao, and B. Z. Wang, "Tunable Topological Edge and Corner States in an All-Dielectric Photonic Crystal," *Optics Express* 30, no. 22 (2022): 40515–40530.

50. Y. C. Zhou, H. S. Lai, J. L. Xie, X. C. Sun, C. He, and Y. F. Chen, "Magnetic Corner States in a Two-Dimensional Gyromagnetic Photonic Crystal," *Physical Review B* 107 (2023): 014105, https://link.aps.org/doi/10.1103/PhysRevB.107.014105.

51. L. Lei, S. Xiao, W. Liu, Q. Liao, L. He, and T. Yu, "Polarization-Independent Second-Order Photonic Topological Corner States," *Physical Review Applied* 20 (2023): 024014, https://link.aps.org/doi/10.1103/PhysRevApplied.20.024014.

52. H. Xing, G. Xu, D. Lu, et al., "Terahertz Topological Photonic Crystals With Dual Edge States for Efficient Routing," *Optics Letters* 48, no. 11 (2023): 2805–2808, https://opg.optica.org/ol/abstract.cfm?URI=ol-48-11-2805.

53. H. Zhang, J. Gao, and D. Xiong, "Realization of Topological Fast and Slow Light Based on Gradient Sandwich Structure," *Optics Express* 32, no. 26 (2024): 46849–46861, https://opg.optica.org/oe/abstract.cfm?URI=oe-32-26-46849.

54. L. Liu, J. G. Hua, X. Zhang, M. H. Lu, and Y. F. Chen, "Acoustic Multiplexing Based on Higher-Order Topological Insulators With Combined Valley and Layer Degrees of Freedom," *Physical Review Applied* 19 (2023): 044055.

55. S. Elshahat, H. Zhang, and C. Lu, "Topological Rainbow Based on Coupling of Topological Waveguide and Cavity," *Optics Express* 31, no. 12 (2023): 20187–20199, https://opg.optica.org/oe/abstract.cfm?URI=oe-31-12-20187.

56. G. J. Tang, X. T. He, F. L. Shi, J. W. Liu, X. D. Chen, and J. W. Dong, "Topological Photonic Crystals: Physics, Designs, and Applications," *Laser & Photonics Reviews* 16, no. 4 (2022): 2100300, https://onlinelibrary.wiley.com/doi/abs/10.1002/lpor.202100300.

57. Y. Liu, S. Leung, and F. F. Li, "Bulk–Disclination Correspondence in Topological Crystalline Insulators," *Nature* 589 (2021): 381–385.

58. X. Zhang, S. Li, Z. Lan, W. Gao, and M. L. N. Chen, "Reconfigurable Photonic Valley Filter in Hybrid Topological Heterostructures," *Laser & Photonics Reviews* 19, no. 3 (2025): 2400797, https://onlinelibrary.wiley.com/doi/abs/10.1002/lpor.202400797.

59. J. Hu, Y. Wang, J. Niu, et al., "Observation of Dual-Polarization Topological Photonic States at Optical Frequencies," *Laser & Photonics*

Reviews 17, no. 12 (2023): 2300515, https://onlinelibrary.wiley.com/doi/abs/10.1002/lpor.202300515.

60. S. Yan, J. Yang, S. Shi, Z. Zuo, C. Wang, and X. Xu, "Transport of a Topologically Protected Photonic Waveguide On-Chip," *Photonics Research* 11, no. 11 (2023): 1021.

61. M. Wang, R. Y. Zhang, L. Zhang, et al., "Topological One-Way Large-Area Waveguide States in Magnetic Photonic Crystals," *Physica; Review Letters* 126 (2021): 067401, https://link.aps.org/doi/10.1103/PhysRevLett.126.067401.

62. Y. Mao, Z. Li, W. Hu, X. Dai, and Y. Xiang, "Topological Slow Light Rainbow Trapping and Releasing Based on Gradient Valley Photonic Crystal," *Journal of Lightwave Technology* 40, no. 15 (2022): 5152–5156.

63. R. Zhou, M. L. N. Chen, X. Shi, et al., "Protected Transverse Electric Waves in Topological Dielectric Waveguides," *IEEE Transactions on Antennas and Propagation* 72, no. 2 (2024): 2058–2063.

64. M. Kim, Z. Jacob, and J. Rho, "Recent Advances in 2D, 3D and Higher-Order Topological Photonics," *Light: Science & Applications* 9 (2020): 130.

65. A. B. Khanikaev and G. Shvets, "Two-Dimensional Topological Photonics," *Nature Photonics* 11 (2017): 763–773.

66. W. Wu, B. Liu, P. He, et al., "A W-Band GSG Probe Fabricated by Metal Additive Manufacturing," *IEEE Transactions on Instrumentation and Measurement* 71 (2022): 1–10.

Supporting Information

Additional supporting information can be found online in the Supporting Information section.

Supporting File: lpor71059-sup-0001-SuppMat.pdf.